JGR Space Physics

RESEARCH ARTICLE

10.1029/2024JA033088

Key Points:

- Radar observations and theory of subauroral sporadic *E* layer irregularities are presented
- Coherent scatter from the layers presents as primary bands of irreguarities with secondary, oblique, braided structure
- Simulations of neutral dynamic instability associated with turning shears in E_s layers consistent with observations

Correspondence to:

D. L. Hysell,
david.hysell@cornell.edu

Citation:

Hysell, D. L., Bui, M. X., & Larsen, M. F. (2024). Observations and model of subauroral sporadic *E* layer irregularities driven by turning shears and dynamic instability. *Journal of Geophysical Research: Space Physics*, *129*, e2024JA033088. https://doi.org/10.1029/2024JA033088

Received 21 JUL 2024
Accepted 5 AUG 2024

Author Contributions:

Conceptualization: D. L. Hysell, M. F. Larsen
Data curation: D. L. Hysell
Formal analysis: D. L. Hysell, M. F. Larsen
Funding acquisition: D. L. Hysell, M. F. Larsen
Investigation: M. X. Bui
Methodology: D. L. Hysell
Project administration: D. L. Hysell, M. F. Larsen
Resources: D. L. Hysell
Software: D. L. Hysell
Supervision: D. L. Hysell
Validation: M. F. Larsen
Visualization: D. L. Hysell
Writing – original draft: D. L. Hysell
Writing – review & editing: D. L. Hysell, M. X. Bui, M. F. Larsen

Observations and Model of Subauroral Sporadic *E* Layer Irregularities Driven by Turning Shears and Dynamic Instability

D. L. Hysell[1], M. X. Bui[1], and M. F. Larsen[2]

[1]Earth and Atmospheric Sciences, Cornell University, Ithaca, NY, USA, [2]Physics and Astronomy, Clemson University, Clemson, SC, USA

Abstract Observations of coherent scatter from patchy sporadic *E* layers in the subauroral zone made with a 30-MHz coherent scatter radar imager are presented. The quasiperiodic (QP) echoes are similar to what has been observed at middle latitudes but with some differences. The echoes arise from bands of scatterers aligned mainly northwest to southeast and propagating to the southwest. A notable difference from observations at middle latitudes is the appearance of secondary irregularities or braids oriented obliquely to the primary bands and propagating mainly northward along them. We present a spectral simulation of the patchy layers that describes neutral atmospheric dynamics with the incompressible Navier Stokes equations and plasma dynamics with an extended MHD model. The simulation is initialized with turning shears in the form of an Ekman spiral. Ekman-type instability deforms the sporadic *E* layer through compressible and incompressible motion. The layer ultimately exhibits both the QP bands and the braids, consequences mainly of primary and secondary neutral dynamic instability. Vorticity due to dynamic instability is an important source of structuring in the sporadic *E* layer.

1. Introduction

Sporadic layers of *E*-region ionization were among the first ionospheric phenomena detected by radio and then radars (Ratcliffe & White, 1934). The layers are composed of metallic ions that diffuse and recombine slowly. They can be at once vertically thin and horizontally expansive. The layers vary with solar, geomagnetic, and meteorological conditions as well as with season for reasons that are not fully understood. They manifest differently at different latitudes. At middle latitudes, they are generally attributed to vertical shear in the horizontal lower thermospheric winds. The impacts of E_s layers, both on the evolution of the ionosphere and on operational communication systems, are widespread, and the literature surrounding the layers is extensive; see reviews by Whitehead (1989); Mathews (1998); Haldoupis (2011); Wu et al. (2021).

That E_s layers could break up and become patchy and unstable at middle latitudes, leading to intense coherent radar scatter, was observed by Riggin et al. (1986) and soon afterward by Yamamoto et al. (1991, 1992) at the newly commissioned MU radar in Japan. Extensive studies from the MU radar revealed the quasiperiodic or 'QP' character of radar backscatter from the patchy layers. The QP phenomenon has been studied widely since by investigators using a variety of ground-based radars (e.g., Pan et al. (1994); Bourdillon et al. (1995); Tsunoda et al. (1998); Hysell and Burcham (1999); Hysell et al. (2004); Saito et al. (2006)) and other radio and optical instruments including ionospheric modification and artificial airglow (e.g., Djuth et al. (1999); Kagan et al. (2000); Bernhardt, Selcher, Siefring, Wilkens, et al. (2005); Bernhardt, Selcher, Siefring, and Gerken (2005); Bernhardt et al. (2006, 2012)). Rocket experiments have shown that the E_s-layer patches are embedded in strong background neutral wind shears and surrounded by polarization electric fields (e.g., (Bernhardt, Selcher, Siefring, Wilkens, et al., 2005; Fukao et al., 1998; Larsen et al., 1998; Yamamoto et al., 1998, 2005)).

A comprehensive program of observations of QP echoes was carried out from St. Croix using a coherent scatter radar imager that shared a common ionospheric volume with the Arecibo Radio Observatory in Puerto Rico (see Hysell et al. (2018) and references therein) (Arecibo is in the subtropics, and observations there reflect strictly midlatitude phenomena, related to but distinct from the emphasis of this paper.) The coherent scatter radar imager gave a plan view of the *E*-region scatterers, disambiguating space and time and revealing their three-dimensional structure. The Arecibo incoherent scatter radar, meanwhile, provided estimates of atmospheric and ionospheric state variables including plasma number density, electric fields, ion composition, and vector neutral wind profiles. The latter were important in view of emerging theories attributing the patchy E_s layers to neutral dynamical instability (as discussed in more detail below).

The salient features of the St. Croix radar observations can be summarized as follows.

1. Echoes were observed starting at *E* region sunset when first blanketing and then patchy, spread sporadic *E* layers were seen by the Arecibo ionosonde.
2. The echoes occurred in clusters separated in time by approximately 40–60 min. Clusters emerged repeatedly throughout the evening, persisting on some occasions nearly until sunrise.
3. Echoes within the clusters presented as regular, diagonal streaks when plotted in range-time-intensity (RTI) format. The regularity of the streaks is responsible for the 'quasiperiodic' terminology although the streaks were not precisely periodic.
4. Radar imagery showed that the streaks were associated with frontal bands of scatterers most often extending from northwest to southeast and propagating to the southwest. There were exceptions to this rule, however. The separation between bands was of the order of tens of km, and propagation speeds were on the order of tens of m/s, resulting in quasi periods on the order of 10 min.
5. The range rates of the echoes could be positive or negative and were indicative of the proper motion of scattering regions within the frontal bands. As the radar line of sight was toward the northwest, the proper motion of the bands could be toward or away from the radar depending on the direction of the background motion.
6. While the signs of the Doppler shifts of the echoes were generally consistent with the signs of the range rates, the magnitudes of the former were generally larger than the latter. Doppler shifts exceeding ±300 m/s were not unusual. These were associated with Farley Buneman instability in metallic ion layers (assuming iron ions and with electron and ion ratios of specific heat of 1 and 5/3, respectively) (Haldoupis et al., 1996).
7. The echoes were collocated with rolls in metallic E_s layers seen by the Arecibo ISR. The ISR further showed that the E_s layers were embedded in steep vertical wind shears that were generally at the threshold for dynamic instability.

Following the demise of the Arecibo radar, a system similar to the St. Croix radar was deployed in Ithaca, NY (42.444° N, 283.498° E, 51.64° geomagnetic latitude). The objective was to seek evidence of QP echoes at higher magnetic latitudes in the subauroral region and near the ionospheric trough. The presence of echoes at higher latitudes would inform QP echo theory (see discussion below). The proximity of Ithaca to the incoherent scatter radar at Millstone Hill would furthermore permit some of the common-volume radar experiments carried out in the Caribbean to be replicated, at least to some degree. Ionosondes at Alpena, MI, and at Millstone Hill are moreover sufficiently close to the volume probed by the Ithaca radar to inform the relationship between QP echoes and blanketing and non-blanketing, patchy, and spread E_s layers over large spatial scales.

QP echoes have been observed frequently by the Ithaca radar in the summer months of 2020 through 2023. The characteristics of the echoes are similar in many respects to what had been observed from St Croix, at least to the extent that verification is possible with the instrumentation available. However, there are a number of important differences.

1. While the intensities have been comparable, echoes have been observed less frequently from Ithaca and for shorter durations. Echoes tend to fill a smaller fraction of the illuminated scattering volume. The excursions of Doppler shifts are also smaller, with no telltales of Farley Buneman instability observed so far. Overall, QP echoes are less robust than in the sub tropics.
2. In addition to the regular QP echo bands, echoes observed from Ithaca frequently exhibit evidence of secondary instabilities forming some time after the primary bands develop. These present as cross-hatches or braids, oriented obliquely to the primary bands. The spacing between secondary irregularities is of the order of several km.

To investigate how the Ithaca radar findings inform QP echo theory, we review theory arising in the aftermath of the MU radar observations and the sounding rocket campaigns that followed. The superficial resemblance of QP echoes to coherent scatter from field aligned irregularities in the equatorial electrojet suggested a role for gradient drift instability. At middle latitudes, however, the fact that the geomagnetic field passes through the layer bottomsides and topsides necessitates a nonlocal mathematical treatment of the instability. Seyler et al. (2004)

showed that gradient drift waves can be unstable at middle latitudes given sufficiently strong forcing but that the dominant horizontal wavelength should be much less than the E_s layer's vertical density scale length. This implies that gradient drift waves are not responsible for the quasiperiodic bands characteristic of QP echoes, although they could well contribute to plasma instability ultimately responsible for the meter-scale plasma waves detected by VHF coherent scatter.

Similar remarks hold for the collisional drift wave instability suggested by Hysell et al. (2013) to explain fine structure in Arecibo E_s layer imagery. This instability derives free energy from the finite density gradient parallel to the geomagnetic field. However, the most unstable drift wave wavelengths are governed by the parallel gradient length scale and expected to be of the order of a few km.

Cosgrove and Tsunoda (2002) identified a plasma instability in midlatitude E_s layers sharing some of the characteristics of the F-region mechanism described by Perkins (1973). Vertical shear in the zonal winds, already a necessary condition for E_s layers to form in the midlatitude E region, is the source of free energy. The assumed planar sheared winds drive meridional currents with opposing directions in the crests and troughs of an initial wavelike perturbation in layer height. Quasineutrality demands the emergence of polarization electric fields in response to the currents, and convection driven by the resulting polarization electric fields accentuates the layer height perturbation, much as with the gradient drift instability. Crucially, however, E_s layers are only unstable for wavelike perturbations propagating in oblique directions with respect to cardinal magnetic coordinates (Zonally propagating waves will not be polarized by the wind-driven meridional currents whereas meridionally propagating waves will not drive convection.) As the fastest growing waves are expected to have wavelengths of a few km to a few tens of km (Cosgrove, 2007), and as oblique propagation directions are preferred, the E_s layer instability is a compelling theory for explaining QP echoes. Numerical simulations supporting the viability of a coupled E/F-region variant of the instability were presented by Yokoyama et al. (2009).

However, Larsen (2000) proposed that the QP echoes are instead a direct consequence of unstable wind shears and neutral dynamical instability, obviating the need for an intermediate, large-scale plasma instability. A number of observations from the Arecibo experiments support this hypothesis. These include the resemblance of the E_s layers to billows and cats eyes (Hysell et al., 2012; Miller & Smith, 1978). Arecibo horizontal wind profiles also supported the proposition of inflection point instability in the lower thermosphere, in agreement with extensive chemical tracer experimental data (Hysell, Larsen, & Sulzer, 2014; Larsen, 2000). Furthermore, all-sky optical images of 557.7 nm neutral emissions were found to coincide spatially with QP echo radar imagery, establishing a direct relationship between large-scale neutral and plasma waves (Hysell et al., 2012; Larsen et al., 2007).

We pursue the neutral wind shear instability QP echo theory on the basis of new observations from the Ithaca radar. After reviewing theory and observations of primary and secondary Kelvin Helmholtz (KH) instability in the mesosphere, Hysell and Larsen (2021) simulated KH in the lower thermosphere driven by planar shear imposed through initial and boundary conditions (see also Bernhardt (2002)). The primary billows arising in 3D simulations were morphologically similar to the banded structures underlying the QP echoes, while secondary instabilities produced features similar to the cross-hatching or braids. Bui et al. (2023) generalized the treatment to the problem of turning shears represented formally by Ekman spirals. Turning shears are more typical of actual conditions in the MLT region but have not been considered in the aforementioned plasma instability treatments. Ekman spirals in particular have multiple unstable eigenmodes and produce rolls that are similar to KH rolls (e.g., Lilly (1966)). In simulations, a combination of primary type-1 and type-2 Ekman instability produced wavefronts similar to the QP echo fronts, and secondary instability produced the braids.

In both of the studies outlined above, the simulations were purely neutral, and the plasma was presumed to follow the incompressible neutral dynamics as a tracer. Below, after reviewing new experimental results from the Ithaca radar, we consider an expanded model that includes neutral dynamics, as contained in the incompressible Navier Stokes equations, and plasma dynamics, as contained in extended MHD theory (see also Chkhetiani and Shalimov (2013)). The extended MHD model includes, among other effects, compressible plasma flow driven by neutral vorticity, which is a primary characteristic of the shear-related neutral instabilities.

2. Observations

Radar echoes from patchy sporadic E layers were observed throughout the summers of 2022 and 2023 from Ithaca, NY, using the 30-MHz coherent scatter radar imager described previously by Hysell and Larsen (2021).

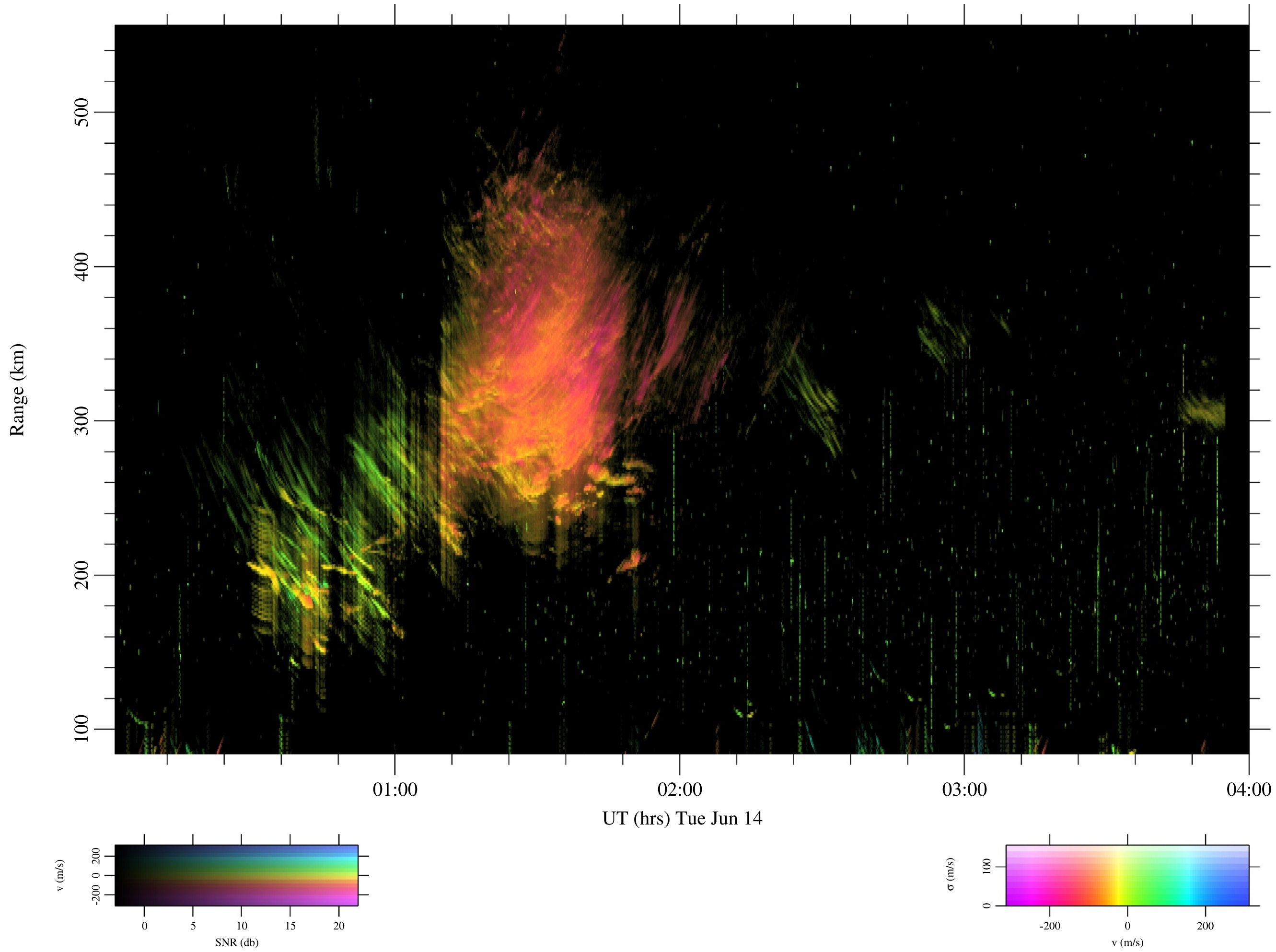

Figure 1. Range time intensity (RTI) representation of radar echoes received on 14 June 2022, versus universal time (LT = UT−5 hr). Pixel brightness, hue, and saturation represent echo signal-to-noise ratio, Doppler shift, and spectral width according to the legends shown. Numerous meteor echoes are visible mainly below about 300 km range. FoEs at Alpena exceeded 8 MHz during this event.

The transmitting antenna array has a 10° beamwidth. The *E* region volume from which coherent backscatter from field-aligned plasma density irregularities can be received lies over southeastern Canada to the east of Lake Huron. As in St. Croix, the main beam of the Ithaca radar is directed toward the northwest. The interpulse period for the observations was 600 km. The corresponding range of Doppler frequencies observable without aliasing is ±625 m/s. The radar employs an 8-kW transmitter and transmits 28-bit maximal-length coded pulses with a range resolution of 1.5 km and a duty cycle of 7%. The measurement cadence is normally 3 s.

Figure 1 shows particularly strong echoes received on 14 June 2022, in conventional range-time-intensity format. As is typical, the echoes present as clusters of narrow streaks. Note that strong radio frequency interference (RFI) accompanied the echoes in this example prior to about 0112 UT, causing atypical signal cutouts at numerous, short time intervals (Interference generally occurs when the maximum useable frequency (MUF) exceeds the 30 MHz radar frequency.) The streaks typical of QP echoes here, meanwhile, are diagonal, with mainly negative and positive range rates (time rates of change of range) before and after about 0115 UT. The range rates in this example can be seen to vary between about ±70 m/s, and the sense of the range rates generally (but not always) agrees with the sign of the Doppler shifts such that approaching (receding) targets are typically blue-shifted (red-shifted). However, the Doppler shifts and range rates do not match quantitatively. In this case, the red shifts exceeded ~150 m/s toward the end of the event around 0200 UT.

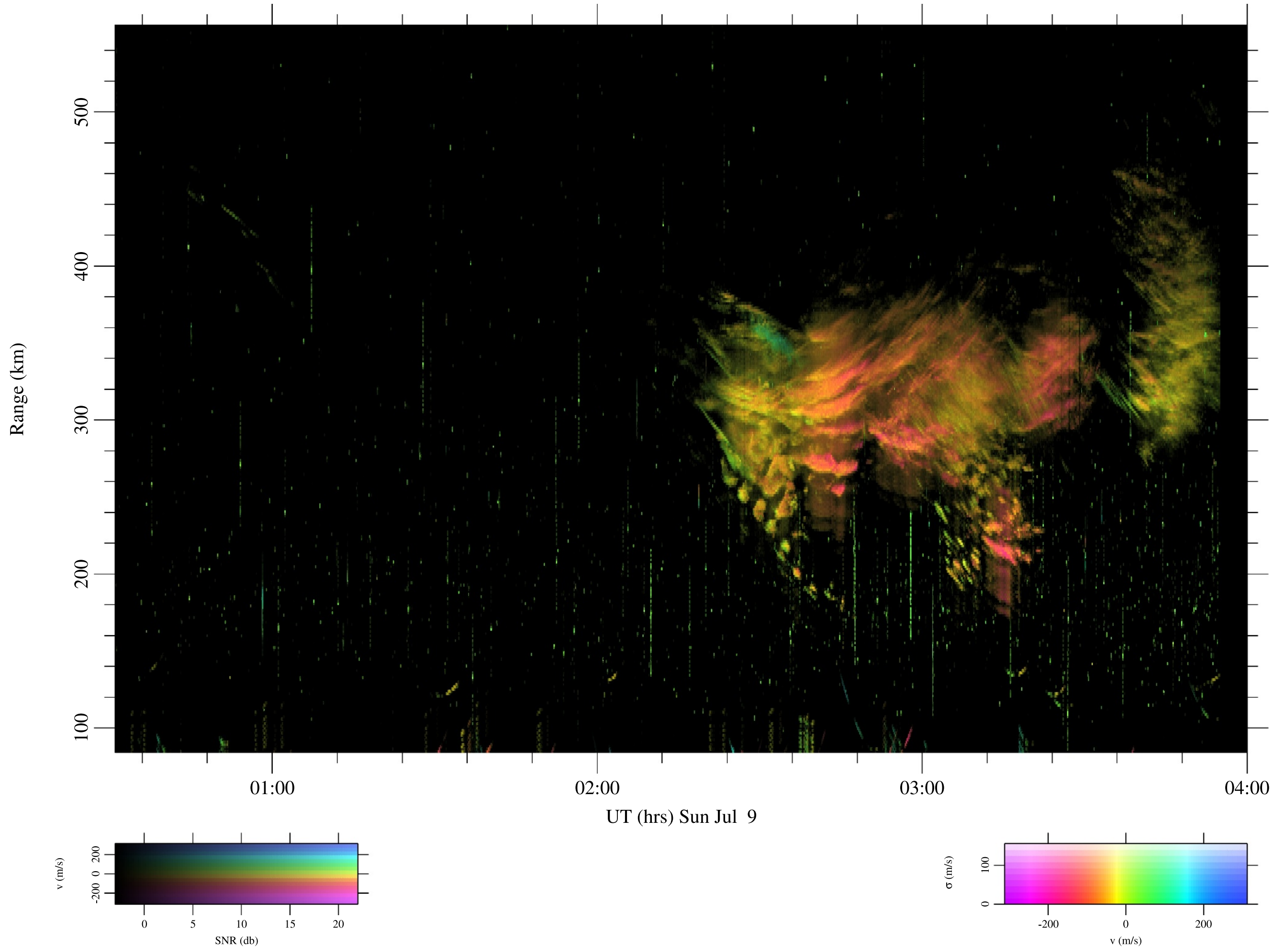

Figure 2. Range time intensity (RTI) representation of radar echoes received on 9 July 2023, versus universal time (LT = UT−5 hr) FoEs at Alpena exceded 8 MHz during this event.

Figure 2 shows another example data set, this time from 9 July 2023. This event exhibits several clusters of streaks between 0200 and 0400 UT with variable but relatively modest range rates and Doppler shifts compared to the previous example. Note that streaks with positive and negative range rates can coexist at times. Radar imaging (see below) reveals that this is just the signature of the spatial superposition of echoes. As in previous studies, we find that the streaks are indicative of the proper motion of scattering regions drifting horizontally through the relatively wide radar antenna beam and sidelobes. Clusters of streaks reflect the fact that scattering regions define individual fronts separated by tens of km in space and fractions of an hour in time.

The Doppler spectra of the echoes observed from Ithaca have been found to be unremarkable, exhibiting symmetric, singly peaked shapes with spectral widths comparable to their Doppler shifts. In the parlance of echoes associated with gradient-drift instability, the echoes would be classified as being 'type 2' (e.g., Farley (2009)) (Note that 'type' has a different meaning when describing Doppler spectra and Ekman instabilities!)

The Ithaca radar uses six spaced antenna groups for reception, the most distant groups being spaced by approximately 15 wavelengths. Interferometry and super-resolution aperture synthesis imaging techniques are used to construct images of the backscatter in the two transverse-to-the-beam directions at every timestep. As all the backscatter arrives from the direction perpendicular to the geomagnetic field, the images are effectively one dimensional but become two dimensional when the range dimension is considered. Images are formed in every Doppler spectral bin and then superimposed.

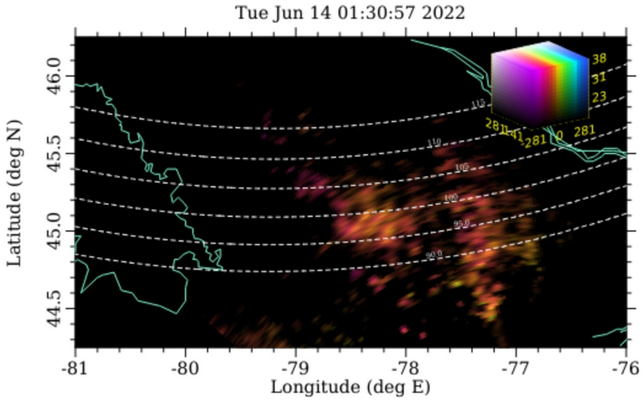

Figure 3. Radar image snapshot from 14 June 2022, at 0130:57 UT. Image pixel brightness, hue, and saturation correspond to echo signal-to-noise ratio, Doppler shift, and spectral width according to the legend shown.

Representative imagery for the 14 June 2022, event at 0130:57 UT is shown in Figure 3. The image depicts two frontal bands of backscatter extended from northwest to southeast and separated by approximately 40 km. Animated sequences of images show that the bands are propagating slowly to the southwest. The echoes are predominately red shifted. A characteristic feature of the echoes is that the bands are broken, with secondary instabilities visible along their length. The secondary irregularities look like cross hatching or braiding. As a rule, they form well after *E*-region sunset, after the frontal bands become well developed, and persist until the bands dissipate.

Figure 4 is from 9 July 2023 at 0239:57 UT. This image is like that from Figure 3 except that it highlights a single frontal band. The secondary structuring or braiding of the band is more distinct in this example, however. The secondary irregularities are spaced by about 5–10 km and are oriented nearly but not quite normally to the primary band. The occurrence of secondary bands of irregularities such as these and those in the previous figure are common features of the E_s layer echoes observed from Ithaca but were only rarely observed by the 30-MHz coherent scatter radar imager deployed for many years on St. Croix.

3. Theory

We consider a three-dimensional model for QP echoes from the midlatitude *E* region including partially coupled neutral and plasma dynamics. The neutral lower thermosphere will be described by the Navier Stokes equations for the incompressible neutral wind velocity **u** in Cartesian coordinates as expressed in Allen and Bridges (2003).

$$\frac{\partial \mathbf{u}}{\partial t} + (\mathbf{u}\cdot\nabla)\mathbf{u} + \frac{1}{R_e}\nabla p + \frac{2}{R_e}\mathbf{u}\times\hat{z} = \frac{1}{R_e}\nabla^2\mathbf{u} \tag{1}$$

$$\nabla\cdot\mathbf{u} = 0 \tag{2}$$

The equations are nondimensionalized using a characteristic length scale $L = 1$ km and a characteristic time scale of $\tau = 10$ s, implying a characteristic speed $v_\circ = L/\tau = 100$ m/s. As in the previous work, we consider a Reynolds number of $R_e = 330$ (e.g., Hickey et al. (2011)) and an Ekman number of $E_k = R_\circ/R_e = 1$ where $R_\circ$ is the Rossby number. For an appropriately specified pressure, Equation 1 has an equilibrium solution referred to as an Ekman spiral which will provide the initial conditions.

$$u_x(z) = \cos(\alpha) - e^{-z}\cos(z-\alpha) \tag{3}$$

$$u_y(z) = \sin(\alpha) + e^{-z}\sin(z-\alpha) \tag{4}$$

$$u_z = 0 \tag{5}$$

$$p(x,y) = p_\circ + 2x\sin(\alpha) - 2y\cos(\alpha) \tag{6}$$

Where α determines the direction of the asymptotic wind. For the purposes of this analysis, the Ekman spiral serves as an expedient proxy for the winds and turning shears often on exhibit in the MLT region.

Instability in Ekman flows under a variety of geographic and flow conditions has been systematically analyzed from multiple mathematical standpoints (see e.g (Coleman et al., 1990; Faller & Kaylor, 1966; Leibovich & Lele, 1985; Lilly, 1966; Mason & Sykes, 1980). Above a Reynolds number of about 55, 'type-2' instability presents as viscous traveling waves with roll axes oriented at about −20° with respect to the asymptotic wind direction. Above a Reynolds number of about 113, meanwhile, a 'type-1' inflection-point instability manifests as stationary waves oriented at about 7° relative

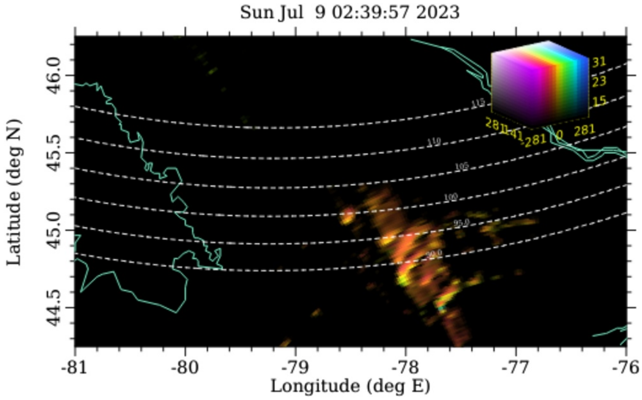

Figure 4. Radar image snapshot from 9 July 2023, at 0239:57 UT.

to the asymptotic (large z) wind direction. Despite having the higher Reynolds number threshold, type-1 instability dominates type-2, having a larger growth rate and a smaller dominant wavelength. Ultimately the rolls produced by instability may saturate to an equilibrium state. Alternatively, if the Reynolds number is large enough, the rolls can lead to three-dimensional secondary instabilities, free energy being drawn from shears along and across the rolls (Dubos et al., 2007). The growth rate of secondary instability is comparable to the primary instability, but the dominant wavelength is about four times smaller.

Bui et al. (2023) simulated the aforementioned primary and secondary Ekman-type instabilities, associating them tentatively with the primary bands and secondary braids in the QP radar imagery. In that study, however, the plasma was treated as a simple tracer of the incompressible neutral flow as a shortcut. Here, we couple the Navier Stokes model to an ionospheric model based on extended MHD. Critically, the model admits compressible plasma flows and the layer deformations that can result.

We consider a continuity equation for an ion-electron gas, a momentum equation, Faraday's law, Ampere's law, and a generalized Ohm's law. We neglect displacement current and electron inertia but retain ion-neutral and electron-neutral collisions, ion and electron pressure, and coupling with the neutral winds. Electrons and ions are taken to be isothermal, and no energy equations are evaluated. The coupling is one way, there being no provision at present to impose ion drag on the neutral dynamics. There is no chemical production or loss.

To nondimensionalize the equations, we make use of τ and L from above. We further introduce $n = n_\circ \tilde{n}$, $\mathbf{B} = B_\circ \widetilde{\mathbf{B}}$, $\mathbf{E} = B_\circ v_\circ \widetilde{\mathbf{E}}$, and $\mathbf{J} = n_\circ e v_\circ \widetilde{\mathbf{J}}$, where $n_\circ$ is the peak background plasma number density and $B_\circ$ the background geomagnetic flux density. Tildes represent nondimensional variables. Written entirely in terms of the nondimensionalized dependent and independent variables and constants, with the tildes omitted for clarity, the extended MHD equations for this model become.

$$\frac{\partial n}{\partial t} + \nabla \cdot (n\mathbf{v}) = 0 \tag{7}$$

$$\frac{\partial}{dt}(n\mathbf{v}) + \nabla \cdot (n\mathbf{v}\mathbf{v}) + v_{cs}^2 \nabla n = \Omega_i \mathbf{J} \times \mathbf{B} - n\nu_{in}(\mathbf{v} - \mathbf{u}) \tag{8}$$

$$\frac{\partial \mathbf{B}}{\partial t} = -\nabla \times \mathbf{E} \tag{9}$$

$$0 = \nabla \times \mathbf{B} - \frac{\Omega_i}{v_a^2}\mathbf{J} \tag{10}$$

$$0 = \mathbf{E} + \mathbf{v} \times \mathbf{B} + \frac{v_{te}^2}{\Omega_e}\frac{\nabla n}{n} - \frac{1}{n}\mathbf{J} \times \mathbf{B} - \frac{\nu_{en}}{\Omega_e}\frac{\mathbf{J}}{n} + \frac{\nu_{en}}{\Omega_{en}}(\mathbf{v} - \mathbf{u}) \tag{11}$$

Where Ω_j is the gyrofrequency for species j, ν_{jn} is the frequency for collisions between neutrals and species j, v_{cs} denotes the isothermal ion acoustic speed, v_a denotes the Alfven speed corresponding to $n_\circ$ and $B_\circ$, and v_{te} denotes the electron thermal speed. Also, $\mathbf{v}$ and $\mathbf{u}$ represent the plasma and neutral drift velocities, respectively.

The numerical simulation is carried out using the Dedalus spectral solver (Burns et al., 2020). Spectral gridding with a Chebychev basis in the vertical and Fourier bases in the horizontal is used. Discretization is via a tau method. Time advance is by mixed implicit-explicit multistep integration obeying the CFL condition. Whereas this approach is well suited to the incompressible Navier Stokes equations, it tends to instability given the extended MHD system with its limited dissipation and tendency to produce discontinuous features. We therefore add anomalous diffusion to Ampere's law (for $\mathbf{B}$) and Ohm's law (for $\mathbf{E}$) to suppress irregularities that would otherwise emerge at the grid scale.

4. Model Results and Interpretation

We use a box size of $L_x = L_y = 40$ in the horizontal and $L_z = 5$ in the vertical, discretized on a grid with $72 \times 72 \times 56$ points. These dimensions represent a computationally expedient compromise, just barely capturing the scales of the primary and secondary irregularities observed by the Ithaca radar. Initial conditions include an Ekman spiral for the winds with a vertical scale length of $L_z/4$ and $\alpha = 90°$. Dirichlet boundary conditions are applied to J_x, J_y, B_z, E_x, E_y at the bottom boundary and to B_x, B_y, E_z at the top boundary and Neumann boundary conditions to B_x, B_y, E_z at the bottom boundary and to B_z, E_x, E_y at the top boundary. All horizontal boundary conditions are periodic. Plasma number density is initialized with a Gaussian layer centered at 3 in the vertical with a width of $\sqrt{5/2}$.

Constant geophysical parameters appropriate for iron E_s layers in the subauroral E region are incorporated in the model. The geomagnetic field is 0.5 G, and the **inclination** is 70°. The ion-neutral and electron-neutral collision frequencies are 300 s^{-1} and 6,000 s^{-1}, respectively, and the temperature is 300 K.

For $\alpha = \pi/2$, the neutral wind is predominantly northward and, crucially, partly westward. The simulation quickly assumes an equilibrium solution with the following characteristics. An eastward electric field arises such as to negate (substantially reduce) the meridional (zonal) current density driven by the winds. The residual westward current density, which depends on the existence of a zonal wind component, is identically solenoidal and increases with altitude with the magnitude of the neutral wind. Considering just the right side of Equation 8, the plasma velocity $\mathbf{v}$ will resemble the wind velocity $\mathbf{u}$ but smaller and with a downward component that increases with altitude. This implies both layer descent and compression.

Considering Equation 11 and neglecting the pressure term, the zonal components imply the eastward electric field essentially balances the westward component of $\mathbf{v} \times \mathbf{B}$.

The agent mainly responsible for compressible ion motion in an incompressible neutral flow is neutral vorticity in the direction of the background magnetic field (e.g., Macleod (1966)). Additionally, Equation 10 demonstrates that the current density must remain solenoidal, the condition for quasineutrality. These mechanisms govern how the plasma behaves as the system departs from its unstable equilibrium.

Results 90 min after initialization are shown in Figure 5 which presents plasma number density, vector electric field, and vertical wind speed in cuts (streamwise and plan views) through the center of the simulation volume. Note that the electric fields are perturbed quantities, the background having been subtracted (Here, the background state is estimated by considering the simulation outputs from 12 min after initialization. This estimate is imperfect but useful for illustrative purposes.)

The figures depict a sporadic E layer being distorted by the neutral flow field mainly through convection which is straightforward in view of the steeply inclined background magnetic field. Neutral rolls associated with type-1 and type-2 Ekman instability have entrained plasma mainly in the bottomside of the layer, which is also becoming more dense and descending under the influence of the background wind shear. In plan view, the plasma density deformations are suggestive of the bands in the Ithaca radar imagery. A superposition of stationary and traveling waves, they propagate slowly and somewhat irregularly to the southwest. In simulation, their combined outer scale increases over time.

In addition, wind vorticity near the rolls causes convergence and divergence in the ion flows, distorting the layer further. The tendency is for divergence within the vortices and convergence between them. Roughly speaking, convergence is expected in regions where w increases from left to right in this figure which are the regions between the vortices. This compressible motion is neglected by QP-echo theories that include wind shears but omit vorticity arising from dynamic instability.

The background westward current density is interrupted in regions of depleted plasma. This leads to the emergence of polarization electric fields which arise to maintain quasineutrality. Figure 6 shows how predominantly westward electric fields emerge roughly in the vicinity of plasma depletions. The correspondence is imperfect in these cuts as different strata of the plasma are connected by highly conducting magnetic field lines with a finite dip angle. Note also that the zonal current density is affected both by layer density and layer altitude since the background-forcing winds vary with height. This also complicates the relationship between the density and the polarization electric field in a 3D volume.

Figure 6 shows simulation results after 165 min. By this time, the E_s later is lower, denser, and more mixed. The mixing, which is partly compressible, has led to homogenization and defeated to large extent any regular, corrugated modulation in the layer height that might otherwise arise from the modulated polarization electric fields. The overall appearance of the layer density in streamwise view in simulation is similar to the way patchy E_s layers present in incoherent scatter data from Arecibo (Hysell et al., 2012). As before, perturbations in the electric

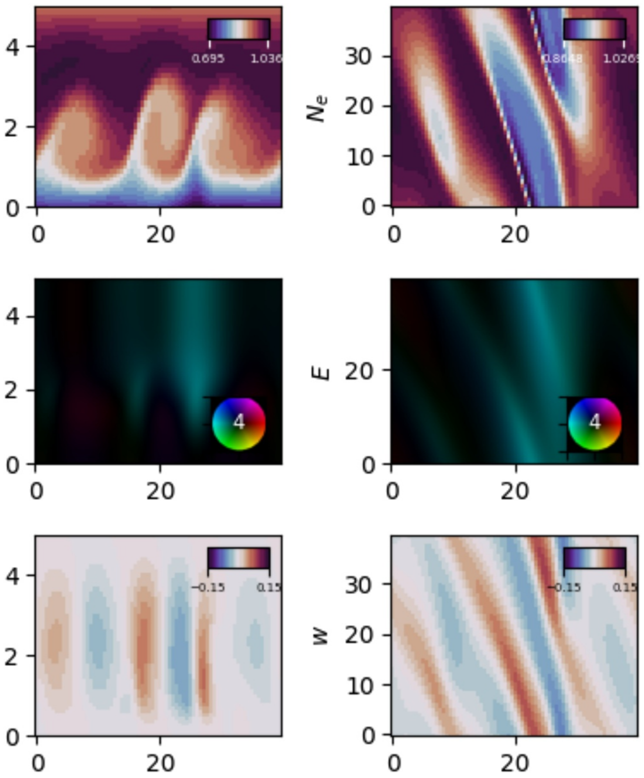

Figure 5. Numerical simulations 90 min after initiation. The left and right columns represent streamwise and plan views, respectively, in cuts through the center of the simulation. The top, middle, and bottom rows represent plasma number density, perturbed vector electric field, and vertical neutral wind speed, respectively. Quantities are non-dimensional (e.g., linear distances are km), and electric fields are plotted as magnitude and direction using a color wheel with a maximum magnitude scale of 4E−2.

field are correlated with perturbations in the plasma density and, to a lesser degree, layer height, most apparently in plan view. The range of hues in the electric field representation in plan view imply rotations in the electric fields required to preserve quasineutrality where both Pedersen and Hall currents are involved (e.g., Hysell and Drexler (2006)).

Crucially, secondary instabilities in the Ekman flow have emerged by this time. Whereas the primary bands are mainly north-south aligned, the secondary braids are almost but not precisely normal to the primaries. The wavelength of the secondaries are approximately a quarter that of the primaries. Over time, the secondary irregularities move with the primaries but also propagate along them and, in this case, mainly northward. The electric field perturbations are dramatic and structured in the vicinity of the secondary instabilities and imply structured electron convection in the direction aligned with the bands. This structure would telegraph directly into the Doppler shifts observed by coherent radar scatter, manifesting mainly as irregular red shifts in the Ithaca experimental configuration.

Overall, the main E_s layer features seen in plan view share many of the characteristics of the imagery collected by the Ithaca radar. This includes the decakilometric broad bands, the narrower, oblique braids, and the apparent motion of both.

5. Analysis and Summary

This paper continues a series of investigations into the role of neutral dynamic instability in the formation of E_s layer irregularities underlying QP echoes. That QP echoes extend to subauroral latitudes where the magnetic dip angle is steep offers insights into the physical processes responsible for them. That Hysell, Munk, and McCarrick (2014) observed QP echoes in Alaska, albeit with the assistance of ionospheric modification techniques, indicates that processes other than convective-type plasma instability are probably not the main agent at work. We may emphasize here that heater-induced FAIs and airglow remain incisive methods for investigating QP echoes at subauroral latitudes further.

QP echoes observed from Ithaca are similar to those observed at middle latitudes if somewhat less common, widespread, and dynamic. This is understandable in view of the fact that the echoes come from the latitudinal boundary of the region where non-auroral E_s layers are found (Yu et al., 2019, 2022). Moreover, as the background magnetic field flux density in the subauroral zone is significantly greater than at middle latitudes, given comparable polarization electric fields, the associated $\mathbf{E} \times \mathbf{B}$ advection speeds and echo Doppler shifts can be expected to be proportionally smaller, and the excitation of Farley Buneman instability less likely. Nonetheless, the echoes can be as strong as their midlatitude relatives. Most notably, they generally exhibit telltales of secondary instability that are uncommon at middle latitudes.

Larsen et al. (2004) first pointed out the analogies between the Ekman flow conditions and the associated Ekman instability in the planetary boundary layer (PBL) and in the mesosphere/thermosphere transition region. Both regions are characterized by a rotational shear with wind speeds increasing with height. In the PBL the winds increase from the no-slip condition at the surface to the geostrophic value at the top of the boundary layer. In the mesosphere/thermosphere transition region, the tides are responsible for the basic rotation of the winds with height, and momentum deposition by breaking gravity waves is primarily responsible for the acceleration that causes the wind speed to increase with height (see, e.g., Liu et al. (2024)). Both are regions of enhanced eddy viscosity capped by more stable altitude ranges. An example of the eddy viscosity variation with height can found in the article by Li et al. (2021). In both the PBL and the high altitude region, the turning shear frequently meets the inflection point criterion that is a requirement for the Ekman instability.

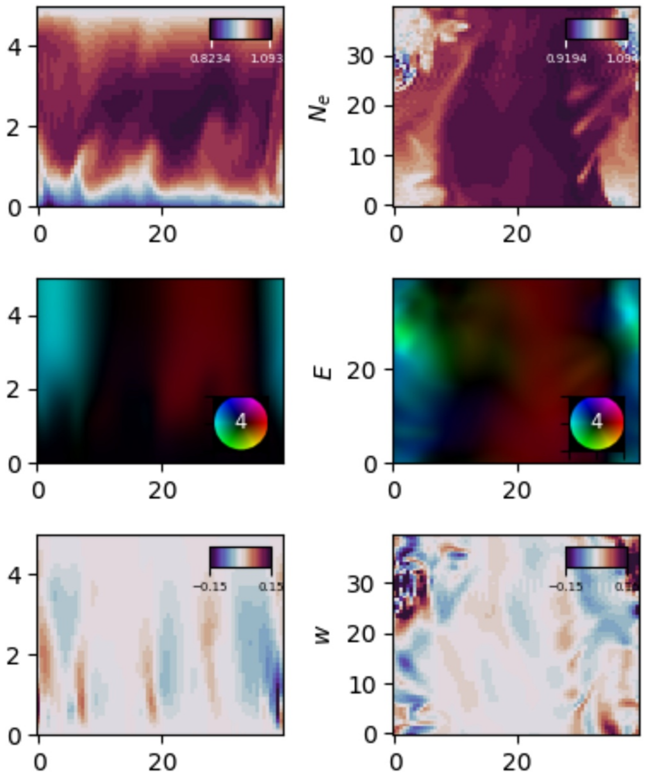

Figure 6. Same as Figure 5 except 165 min after initiation.

In the mesosphere, as is the case in the PBL, the eddy viscosity will vary both with time and height as the upward propagating gravity waves break at different heights and different times. The Ekman instability has been found to be remarkably robust and consistent, even in the case of such variations (see, e.g., Momen and Bou-Zeid (2017) and Ionescu-Kruse (2021)). These analyses give us confidence that simulations of the Ekman instability in the mesosphere/thermosphere transition region are relevant even with the various approximations that have to be made.

In combined neutral-plasma numerical simulations initialized with Ekman spiral background flows (i.e., with turning shears), Ekman-type instabilities produce bands of rolls and smaller-scale secondary ripples that are morphologically similar, respectively, to the QP-echo bands and braids observed from Ithaca. Moreover, the simulations show that the plasma responds to the neutral forcing through simple field-aligned convection but also through compressible motion resulting from neutral vorticity in the direction of the geomagnetic field. This distorts the E_s layers, affecting their morphology and modulating the transverse electric field in complicated ways. The response of the plasma is better described as mixing and compression than corrugation and simple plane wave growth. The key point is that the rolls produced by neutral shear flow and dynamic instability affect plasma evolution in a fundamentally different way than neutral shear alone.

The analysis presented here falls short of accounting for the 5-m plasma density irregularities responsible for the 30 MHz coherent scatter making a quantitative assessment of the echo Doppler spectra. We provisionally attribute the 5-m waves to gradient drift and/or drift wave instability operating at scales between meter scales and the simulation grid scales. As for the Doppler shifts of the coherent scatter, we assume that the real part of the linear dispersion relation for gradient drift waves applies, as it is simply consistent with the conversation of mass and momentum and with quasineutrality in the E region (e.g., Fejer and Kelley (1980)). The Doppler shift in that case is expected to be a hybrid of the line-of-sight electron ($\mathbf{E} \times \mathbf{B}$) and ion drift velocities with a proportionality constant that decreases with decreasing altitude. We may expect it to mirror but depart from the range rate of the echoes which is presumably governed by the line-of-sight ion drift speed. The larger the electric field, the larger the departure. The more intense the plasma density perturbation, the larger the electric field, and the greater the departure.

This analysis also omitted the effects of ion drag on the neutral dynamics. In the future, this can be included simply by introducing the $\mathbf{J} \times \mathbf{B}$ force back into the Navier Stokes equations (e.g., Song et al. (2001)). Doing so may reveal why certain propagation directions are more likely in nature than others as the drag on neutral waves is a strong function of propagation direction with respect to the geomagnetic field (Kelley, 2011). The analysis further neglects any treatment of neutral turbulence-mean-flow interactions which should influence the late-stage development of the E_s-layer irregularities (e.g., Reif et al. (2002)).

Data Availability Statement

Data used for this paper are available through Hysell (2024).

Acknowledgments
The work was supported by NSF awards AGS-2011304 to Cornell University and AGS-2012994 to Clemson University.

References

Allen, L., & Bridges, J. (2003). Hydrodynamic stability of the Ekman boundary layer including interaction with a compliant surface: A numerical framework. *European J. of Mech. B/Fluids*, *22*(3), 239–258. https://doi.org/10.1016/s0997-7546(03)00036-0

Bernhardt, P. A. (2002). The modulation of sporadic-E layers by Kelvin-Helmholtz billows in the neutral atmosphere. *Journal of Atmospheric and Solar-Terrestrial Physics*, *64*(12–14), 1487–1504. https://doi.org/10.1016/s1364-6826(02)00086-x

Bernhardt, P. A., Selcher, C. A., Siefring, C. L., & Gerken, E. (2005a). Glow imaging of ionospheric density structures and plasma drifts with artificial illumination by high power radio waves. *IEEE Transactions on Plasma Science*, *33*(2), 504–505. https://doi.org/10.1109/tps.2005.845917

Bernhardt, P. A., Selcher, C. A., Siefring, C. L., Wilkens, M., Compton, C., Yamamoto, M., et al. (2005b). Radio tomographic imaging of sporadic E-layers during SEEK2. *Annals of Geophysics*, *23*(7), 2357–2368. https://doi.org/10.5194/angeo-23-2357-2005

Bernhardt, P. A., Werne, J., & Larsen, M. F. (2006). Characterizing the ionosphere. Meeting Proceedings RTO-MP-IST-056. *Neuilly-sur-Seine, France*, *34*.

Bernhardt, P. A., Wong, M., Huba, J. D., Fejer, B. G., Wagner, L. S., Goldstein, J. A., et al. (2012). Optical remote sensing of the thermosphere with HF pumped artificial airglow. *Journal of Geophysical Research*, *105*(A5), 10657–10671. https://doi.org/10.1029/1999JA000366

Bourdillon, A., Haldoupis, C., & Delloue, J. (1995). High-frequency Doppler radar observations of magnetic aspect sensitive irregularities in the midlatitude *E* region ionosphere. *Journal of Geophysical Research*, *100*(21), 503–21521. https://doi.org/10.1029/95ja01079

Bui, M. X., Hysell, D. L., & Larsen, M. F. (2023). Midlatitude sporadic E-layer horizontal structuring modulated by neutral instability and mixing in the lower thermosphere. *Journal of Geophysical Research*, *128*(2), e2022JA030929. https://doi.org/10.1029/2022JA030929

Burns, K. J., Vasil, G. M., Oishi, J. S., Lecoanet, D., & Brown, B. P. (2020). Dedalus: A flexible framework for numerical simulations with spectral methods. *Physical Review Research*, *2*(2), 023068. 1–39, 2643-1564/2020. https://doi.org/10.1103/physrevresearch.2.023068

Chkhetiani, O. G., & Shalimov, S. L. (2013). Mechanism by which frontal structures in the ionospheric sporadic *E* layers are formed. *Geomagnetism and Aeronomy*, *53*(2), 177–187. https://doi.org/10.1134/s0016793213020059

Coleman, G., Ferziger, J., & Spalart, P. (1990). A numerical study of the turbulent Ekman layer. *Journal of Fluid Mechanics*, *213*(-1), 742–757. https://doi.org/10.1017/s0022112090002348

Cosgrove, R. B. (2007). Wavelength dependence of the linear growth rate of the *Es* layer instability. *Annals of Geophysics*, *25*(6), 1311–1322. https://doi.org/10.5194/angeo-25-1311-2007

Cosgrove, R. B., & Tsunoda, R. T. (2002). A direction-dependent instability of sporadic- *E* layers in the nighttime midlatitude ionosphere. *Geophysical Research Letters*, *29*(18), 1864. https://doi.org/10.1029/2002JA009728

Djuth, F. T., Bernhardt, P. A., Tepley, C. A., Gardner, J. A., Kelley, M. C., Broadfoot, A. L., et al. (1999). Production of large airglow enhancements via wave-plasma interactions in sporadic-E. *Geophysical Research Letters*, *26*(11), 1557–1560. https://doi.org/10.1029/1999gl900296

Dubos, T., Barthlott, C., & Drobinski, P. (2007). Emergence of secondary instability of Ekman layer rolls. *Journal of the Atmospheric Sciences*, *65*(7), 2326–2342. https://doi.org/10.1175/2007jas2550.1

Faller, A., & Kaylor, R. (1966). A numerical study of the instability of the laminar Ekman boundary layer. *Journal of the Atmospheric Sciences*, *23*(5), 466–480. https://doi.org/10.1175/1520-0469(1966)023<0466:ansoti>2.0.co;2

Farley, D. T. (2009). The equatorial *E*-region and its plasma instabilities: A tutorial. *Annals of Geophysics*, *27*(4), 1509–1520. https://doi.org/10.5194/angeo-27-1509-2009

Fejer, B. G., & Kelley, M. C. (1980). Ionospheric irregularities. *Reviews of Geophysics*, *18*(2), 401–454. https://doi.org/10.1029/rg018i002p00401

Fukao, S., Yamamoto, M., Tsunoda, R. T., Hayakawa, H., & Mukai, T. (1998). The SEEK (sporadic- *E* experiment over Kyushu) campaign. *Geophysical Research Letters*, *25*(11), 1761–1764. https://doi.org/10.1029/98gl00932

Haldoupis, C. (2011). Midlatitude sporadic *E*: A typical paradigm of atmosphere-ionosphere coupling. *Space Science Reviews*, *168*(1–4), 441–461. https://doi.org/10.1007/s11214-011-9786-8

Haldoupis, C., Schlegel, K., & Farley, D. T. (1996). An explanation for type 1 radar echoes from the midlatitude *E*-region ionosphere. *Geophysical Research Letters*, *23*, 97–100. https://doi.org/10.1029/95gl03585

Hickey, M. P., Walterscheid, R. L., & Schubert, G. (2011). Gravity wave heating and cooling of the thermosphere: Sensible heat flux and viscous flux of kinetic energy. *Journal of Geophysical Research*, *116*, A12326. https://doi.org/10.1029/2011JA016792

Hysell, D. L. (2024). Cornell coherent scatter radar imager data repository. [Dataset]. https://doi.org/10.7298/8sxf-b977

Hysell, D. L., & Burcham, J. (1999). HF radar observations of quasiperiodic *E* layer echoes over North America. *Journal of Geophysical Research*, *104*, 4361.

Hysell, D. L., & Drexler, J. (2006). Polarization of *E* region plasma irregularities. *Radio Science*, *41*(4), RS4015. https://doi.org/10.1029/2005RS003424

Hysell, D. L., & Larsen, M. F. (2021). VHF imaging radar observations and theory of banded midlatitude sporadic *E* ionization layers. *Journal of Geophysical Research: Space Physics*, *126*(5), e2021JA029257. https://doi.org/10.1029/2021JA029257

Hysell, D. L., Larsen, M. F., Fritts, D. C., Laughman, B., & Sulzer, M. P. (2018). Major upwelling and overturning in the mid-latitude F region ionosphere. *Nature Communications*, *9*(3326), 3326. https://doi.org/10.1038/s41467-018-05809-x

Hysell, D. L., Larsen, M. F., & Sulzer, M. P. (2014a). High time and height resolution neutral wind profile measurements across the mesosphere/lower thermosphere region using the Arecibo incoherent scatter radar. *Journal of Geophysical Research*, *119*(3), 2345–2358. https://doi.org/10.1002/2013JA019621

Hysell, D. L., Larsen, M. F., & Zhou, Q. H. (2004). Common volume coherent and incoherent scatter radar observations of mid-latitude sporadic *E*-layers and QP echoes. *Annals of Geophysics*, *22*(9), 3277–3290. https://doi.org/10.5194/angeo-22-3277-2004

Hysell, D. L., Munk, J., & McCarrick, M. (2014b). Sporadic *E* ionization layers observed with radar imaging and ionospheric modification. *Geophysical Research Letters*, *41*(20), 6987–6993. https://doi.org/10.1002/2014GL061691

Hysell, D. L., Nossa, E., Aveiro, H. C., Larsen, M. F., Munro, J., Sulzer, M. P., & González, S. A. (2013). Fine structure in midlatitude sporadic *E* layers. *Journal of Atmospheric and Solar-Terrestrial Physics*, *103*, 16–23. https://doi.org/10.1016/j.jastp.2012.12.005

Hysell, D. L., Nossa, E., Larsen, M. F., Munro, J., Smith, S., Sulzer, M. P., & González, S. A. (2012). Dynamic instability in the lower thermosphere inferred from irregular sporadic layers. *Journal of Geophysical Research*, *117*, A8. https://doi.org/10.1029/2012JA017910

Ionescu-Kruse, D. (2021). Analytical atmospheric Ekman-type solutions with height-dependent eddy viscosity. *Journal of Mathematical Fluid Mechanics*, *23*(010001–11), 6928. https://doi.org/10.1007/s00021-020-00543-1

Kagan, L. M., Kelley, M. C., Garcia, F., Bernhardt, P. A., Djuth, F. T., Sulzer, M. P., & Tepley, C. A. (2000). The structure of electromagnetic wave-induced 557.7-nm emission associated with a sporadic-E event over Arecibo. *Physical Review Letters*, *85*(1), 218–221. https://doi.org/10.1103/physrevlett.85.218

Kelley, M. C. (2011). On the origin of mesoscale TIDs at midlatitudes. *Annals of Geophysics*, *29*(2), 361–366. https://doi.org/10.5194/angeo-29-361-2011

Larsen, M. F. (2000). A shear instability seeding mechanism for quasi-periodic radar echoes. *Journal of Geophysical Research*, *105*(A11), 24931–24940. https://doi.org/10.1029/1999ja000290

Larsen, M. F., Fukao, S., Yamamoto, M., Tsunoda, R., Igarashi, K., & Ono, T. (1998). The SEEK chemical release experiment: Observed neutral wind profile in a region of sporadic- *E*. *Geophysical Research Letters*, *25*(11), 1789–1792. https://doi.org/10.1029/98gl00986

Larsen, M. F., Hysell, D. L., Zhou, Q. H., Smith, S. M., Friedman, J., & Bishop, R. L. (2007). Imaging coherent scatter radar, incoherent scatter radar, and optical observations of quasiperiodic structures associated with sporadic *E* layers. *Journal of Geophysical Research*, *112*(A6), A06321. https://doi.org/10.1029/2006JA012051

Larsen, M. F., Liu, A. Z., Gardner, C. S., Kelley, M. C., Collins, S., Friedman, J., & Hecht, J. H. (2004). Observations of overturning in the upper mesosphere and lower thermosphere. *Journal of Geophysical Research*, *109*(D2), D02S04. https://doi.org/10.1029/2002JD003067

Leibovich, S., & Lele, S. (1985). The influence of the horizontal component of the earth's angular velocity on the instability of the Ekman layer. *Journal of Fluid Mechanics*, *150*, 41–87. https://doi.org/10.1017/s0022112085000039

Li, J., Collins, R., Lu, X., & Williams, B. (2021). Lidar observations of instability and estimates of vertical eddy diffusivity induced by gravity wave breaking in the Arctic mesosphere. *Journal of Geophysical Research: Atmospheres*, *126*, e2020JD033450. https://doi.org/10.1029/2020JD033450

Lilly, D. K. (1966). On the instability of Ekman boundary flow. *Journal of the Atmospheric Sciences*, *23*(5), 481–494. https://doi.org/10.1175/1520-0469(1966)023<0481:otioeb>2.0.co;2

Liu, H.-L., Lauritzen, P. H., & Vitt, F. (2024). Impacts of gravity waves on the thermospheric circulation and composition. *Geophysical Research Letters*, *51*(3), e2023GL107453. https://doi.org/10.1029/2023GL107453

Macleod, M. A. (1966). Sporadic E theory: I. Collision-Geomagnetic equilibrium. *Journal of Atmospheric and Terrestrial Physics*, *23*(1), 96–109. https://doi.org/10.1175/1520-0469(1966)023<0096:seticg>2.0.co;2

Mason, P., & Sykes, R. (1980). A two-dimensional numerical study of horizontal roll vortices in the neutral atmospheric boundary layer. *Quart. J. Roy. Meteor. Soc.*, *106*(448), 351–366. https://doi.org/10.1002/qj.49710644808

Mathews, J. D. (1998). Sporadic E: Current views and recent progress. *Journal of Atmospheric and Solar-Terrestrial Physics*, *4*, 413–435. https://doi.org/10.1016/s1364-6826(97)00043-6

Miller, K. L., & Smith, L. G. (1978). Incoherent scatter radar observations of irregular structure in mid-latitude sporadic *E* layers. *Journal of Geophysical Research*, *83*(A8), 3761–3775. https://doi.org/10.1029/ja083ia08p03761

Momen, M., & Bou-Zeid, E. (2017). Analytical reduced models for the non-stationary diabatic atmospheric boundary layer. *Boundary-Layer Meteorology*, *164*(3), 383–399. https://doi.org/10.1007/s10546-017-0247-0

Pan, C. J., Liu, C. H., Röttger, J., & Su, S. Y. (1994). A three dimensional study of *E* region irregularity patches in the equatorial aeronomy region using the Chung-Li VHF radar. *Geophysical Research Letters*, *21*(17), 1763–1766. https://doi.org/10.1029/94gl01195

Perkins, F. (1973). Spread *F* and ionospheric currents. *Journal of Geophysical Research*, *78*(1), 218–226. https://doi.org/10.1029/ja078i001p00218

Ratcliffe, J. A., & White, E. L. C. (1934). Some automatic records of wireless waves reflected from the ionosphere. *Proceedings of the Physical Society*, *46*(1), 107–115. https://doi.org/10.1088/0959-5309/46/1/310

Reif, B. A. P., Werne, J., Andreassen, Ø., Meyer, C., & Davis-Mansour, M. (2002). Entrainment-zone restratification and flow structures in stratified shear turbulence. Center for Turbulence Research. *Proceedings of the Summer Program*, 245–256.

Riggin, D., Swartz, W. E., Providakes, J., & Farley, D. T. (1986). Radar studies of long-wavelength waves associated with mid-latitude sporadic *E* layers. *Journal of Geophysical Research*, *91*(A7), 8011–8024. https://doi.org/10.1029/ja091ia07p08011

Saito, S., Yamamoto, M., Hashiguchi, H., & Maegawa, A. (2006). Observation of three-dimensional signatures of quasi-periodic echoes associated with mid-latitude sporadic-E layers by MU radar ultra-multi-channel system. *Geophysical Research Letters*, *33*(14), L14109. https://doi.org/10.1029/2005GL025526

Seyler, C. E., Rosado-Roman, J. M., & Farley, D. T. (2004). A nonlocal theory of the gradient-drift instability in ionospheric plasmas at mid-latitudes. *Journal of Atmospheric and Solar-Terrestrial Physics*, *66*(17), 1627–1637. https://doi.org/10.1016/j.jastp.2004.07.011

Song, P., Gombosi, T. I., & Ridley, A. J. (2001). Three-fluid Ohm's law. *Journal of Geophysical Research*, *106*(A5), 8156. https://doi.org/10.1029/2000ja000423

Tsunoda, R. T., Fukao, S., Yamamoto, M., & Hamasaki, T. (1998). First 24.5 MHz radar measurements of quasiperiodic backscatter from field-aligned irregularities in midlatitude sporadic *E*. *Geophysical Research Letters*, *25*(11), 1765–1768. https://doi.org/10.1029/98gl01086

Whitehead, J. D. (1989). Recent work on mid-latitude and equatorial sporadic *E*. *Journal of Atmospheric and Terrestrial Physics*, *51*(5), 401–424. https://doi.org/10.1016/0021-9169(89)90122-0

Wu, J., Feng, W., Liu, H.-L., Xue, X., Marsh, D. R., & Plane, J. M. C. (2021). Self-consistent global transport of metallic ions with WACCM-X. *Atmospheric Chemistry and Physics*, *21*(15), 15619–15630. https://doi.org/10.5194/acp-21-15619-2021

Yamamoto, M., Fukao, S., Ogawa, T., Tsuda, T., & Kato, S. (1992). A morphological study of mid-latitude *E*-region field-aligned irregularities observed with the MU radar. *Journal of Atmospheric and Terrestrial Physics*, *54*(6), 769–777. https://doi.org/10.1016/0021-9169(92)90115-2

Yamamoto, M., Fukao, S., Tsunoda, R. T., Pfaff, R., & Hayakawa, H. (2005). SEEK-2 (sporadic- *E* experiment over Kyushu 2) – Project outline. *Annals of Geophysics*, *23*(7), 2295–2305. https://doi.org/10.5194/angeo-23-2295-2005

Yamamoto, M., Fukao, S., Woodman, R. F., Ogawa, T., Tsuda, T., & Kato, K. (1991). Mid-latitude *E* region field-aligned irregularities observed with the MU radar. *Journal of Geophysical Research*, *96*(15), 943–15949. https://doi.org/10.1029/91ja01321

Yamamoto, M., Ono, T., Oya, H., Tsunoda, R. T., Larsen, M. F., Fukao, S., & Yamamoto, M. (1998). Structures in sporadic- *E* observed with an impedance probe during the SEEK campaign: Comparisons with neutral-wind and radar-echo observations. *Geophysical Research Letters*, *25*(11), 1781–1784. https://doi.org/10.1029/98gl00709

Yokoyama, T., Hysell, D. L., Otsuka, Y., & Yamamoto, M. (2009). Three-dimensional simulation of the coupled Perkins and Es-layer instabilities in the nighttime midlatitude ionosphere. *Journal of Geophysical Research*, *114*, A03308. https://doi.org/10.1029/2008JA013789

Yu, B., Xue, X., Scott, C. J., Yue, X., & Dou, X. (2022). An empirical model of the ionospheric sporadic E layer based on GNSS radio occultation data. *Space Weather*, *20*(8), e2022SW003113. https://doi.org/10.1029/2022SW003113

Yu, B., Xue, X., Yue, X., Yang, C., Yu, C., Dou, X., et al. (2019). The global climatology of the intensity of the ionospheric sporadic *E* layer. *Atmospheric Chemistry and Physics*, *19*(6), 4139–4151. https://doi.org/10.5194/acp-19-4139-2019